ACS Energy LETTERS

Cite This: ACS Energy Lett. 2019, 4, 2508−2513

http://pubs.acs.org/journal/aelccp

LETTER

Hot Electron Emission in Plasmonic Thermionic Converters

Shengxiang Wu,[†] Nicki Hogan,[†] and Matthew Sheldon*[,†,‡]

[†]Department of Chemistry, Texas A&M University, College Station, Texas 77843-3255, United States

[‡]Department of Material Science and Engineering, Texas A&M University, College Station, Texas 77843-3255, United States

Supporting Information

ABSTRACT: Thermionic converters generate electricity from thermal energy in a power cycle based on the vacuum emission of electrons. While thermodynamically efficient, practical implementations are limited by the extreme temperatures required for electron emission (>1500 K). Here we show how metal nanostructures that support resonant plasmonic absorption enable an alternative strategy. The high temperatures required for efficient vacuum emission can be maintained in a subpopulation of photoexcited "hot" electrons during steady-state optical illumination, whereas the lattice temperature of the metal remains within the range of thermal stability, below 600 K. We have also developed an optical thermometry technique based on anti-Stokes Raman spectroscopy that confirms these unique electron dynamics. Thermionic devices constructed from optimized plasmonic absorbers show performance that can outcompete other strategies of concentrated solar power conversion in terms of efficiency and thermal stability.

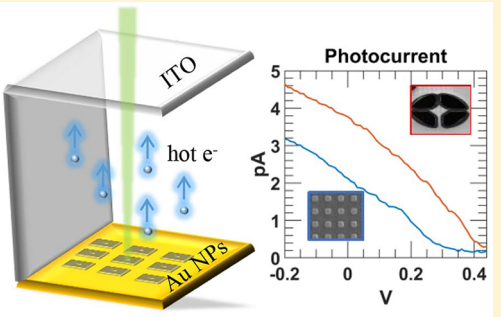

Metals that support surface plasmons, the coherent oscillations of free electrons, provide efficient coupling of electromagnetic radiation to extremely confined subwavelength "hot spots" at nanoscale edges and corners. Strong resonant optical absorption via Landau damping generates a large transient population of photoexcited electron−hole pairs at these hot spots in the metal.[1] The photoexcited carriers relax quickly, first through electron−electron scattering (approximately femtoseconds) to form a thermal distribution of "hot" electrons at a significantly elevated temperature compared with the lattice. On a slower time scale (approximately picoseconds), electrons relax by scattering with phonons, resulting in the local photothermal heating of the lattice.[1] There has recently been significant interest in taking advantage of the high kinetic energy of these hot electrons before they thermalize with the lattice for applications in photodetection,[2] optical energy conversion,[3,4] and catalysis.[5,6] In addition to the short lifetime, one major challenge is the limited escape cone of hot electron trajectories with suitable momentum to exit the metal. Notably, nanoscopic confinement increases the probability that a hot electron will reach a surface with appropriate momentum for collection in an external device or chemical reaction.[7,8]

In this Letter, we show how the extraordinary photophysics of plasmonic hot electrons is particularly well suited for optoelectronic power conversion based on thermionic power cycles. In a thermionic converter, a metal cathode emitter is brought to high temperature so that a significant fraction of the electrons has kinetic energy greater than the metal's work function. Electrons are vacuum-emitted and collected at a lower temperature anode to generate electrical power. In principle, thermionic converters have theoretical efficiencies that far exceed thermoelectric or mechanical energy converters.[9] In practice, the large energy barrier of the work function impedes electron emission unless temperatures exceed ∼1500 K. This high-temperature requirement has hindered the practical application of the technology, which was historically explored for concentrated solar−thermal power generation[9,10] and more recently explored in conjunction with hybrid photovoltaic schemes.[11,12] However, the approximately 100 times smaller heat capacity of the electron gas in metals[13] compared with the lattice entails that nanostructured plasmonic absorbers can maintain a subpopulation of hot electrons at a temperature greatly in excess of the lattice during steady-state illumination. Thus optimized nanostructures can be used to effectively decouple the high kinetic energy electrons required for efficient thermionic emission while maintaining lattice temperatures compatible with the thermal tolerance of the metal.

In efforts to quantitatively understand the role of photoexcited electrons during thermionic power conversion, we have developed an optical thermometry technique based on anti-Stokes Raman spectroscopy that simultaneously determines the lattice temperature, the hot electron temperature, and the

Received: August 23, 2019
Accepted: September 19, 2019
Published: September 19, 2019

DOI: 10.1021/acsenergylett.9b01857
ACS Energy Lett. 2019, 4, 2508−2513

size of the subpopulation of hot electrons during steady-state illumination. Under optical powers spanning 10^6 to 10^{10} Wm^{-2} on nanostructured gold, we observe lattice temperatures between 300 and 600 K, whereas up to 8% of the electron gas is maintained at temperatures well above 1500 K. When these illuminated plasmonic absorbers are used as cathodes in thermionic power converters, we indeed observe optical-to-electrical power conversion consistent with the electronic temperature and no evidence of thermal degradation. Moreover, we confirm that this unique mechanism for decoupling electronic and lattice temperature overcomes challenges that have impeded other thermionic strategies for concentrated solar thermal power conversion.

Top-down lithographic techniques were used to fabricate a 90 μm square array of 225 nm × 225 nm × 100 nm gold nanocubes at a pitch of 500 nm on a 150 nm thick gold film, as displayed in Figure 1b. The structure provides strong field

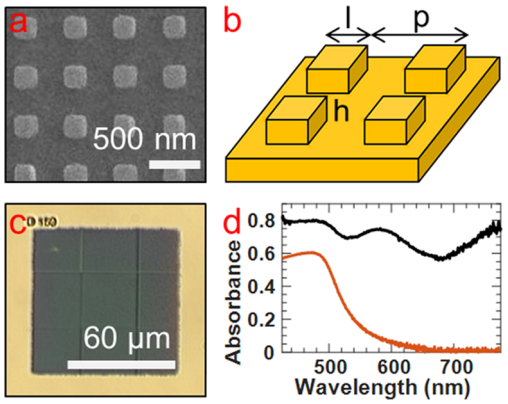

Figure 1. (a) SEM image of the fabricated nanostructure. (b) Schematic of the unit cell with l = 225 nm, p = 500 nm, and h = 100 nm on a 150 nm thick gold film. (c) Optical image of the fabricated nanostructure. (d) Absorbance of the nanostructure (black) compared with a smooth gold thin film with a thickness of 150 nm (red).

concentration at hot spots on the nanocubes where there is greater surface area intersecting escape cones for hot electron emission.[14] (See eqs S3 and S4 in the SI.) Scanning electron microscope (SEM) and optical images are displayed in Figure 1a,c. At the excitation wavelength (532 nm) there is an approximate two-fold increase in absorption compared with a gold thin film (Figure 1d), leading to increased photothermalization localized in the nanocubes.

Temperature measurements during photothermalization were achieved by collecting anti-Stokes Raman spectra under 532 nm continuous-wave (CW) laser illumination. A representative anti-Stokes spectrum is shown in Figure 2a. The signal from the nanostructure is ten times larger than that from a gold thin film, comparable to enhancements observed in surface-enhanced Raman studies.[15] Direct scattering from phonons does not contribute to the Raman signal from noble metals;[16] therefore, the broad frequency response is due to a direct anti-Stokes interaction with the electron gas. The physical origin of this anti-Stokes signal is still under some debate, with recent studies providing evidence that the signal may be due to photoluminescence rather than coherent scattering, as in conventional Raman spectroscopy.[17] Regardless of the microscopic mechanism, the spectral-dependent intensity of the anti-Stokes spectrum has been established as an

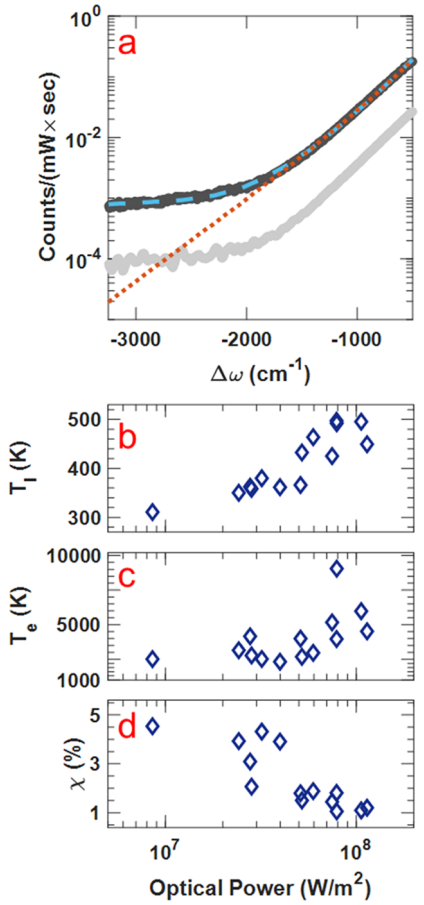

Figure 2. (a) Measured anti-Stokes Raman signal from the nanostructure (solid black) and gold thin film (solid gray) in atmosphere, both collected under 7.3 × 10^9 Wm^{-2} 532 nm laser excitation. The fit to a one-temperature model (eq 1, red dotted line) and a two-temperature model (eq 2, blue dashed line) are shown. The one-temperature fit gives T_l = 459 K, whereas the two-temperature fit gives T_l = 430 K, T_e = 10 040 K, and χ = 0.34%. The TTM fit for (b) lattice temperature, (c) electronic temperature, and (d) the percentage of hot electrons for the nanostructure under vacuum.

accurate indicator of the lattice temperature of a noble metal.[18−21] The anti-Stokes signal intensity therefore follows the Bose−Einstein thermal distribution of lattice excitations, as in eq 1.

$$I(\Delta\omega) = C * D(\Delta\omega) * \left(\frac{1}{e^{hc\Delta\omega/kT_l} - 1} \right) \quad (1)$$

Here I is the anti-Stokes signal intensity normalized by power and integration time as a function of the energy difference, $\Delta\omega$, from the Rayleigh line in m^{-1}, and T_l is the lattice temperature in Kelvins. This expression includes a constant scaling factor, C, to account for the experimental collection efficiency that is recalibrated for each measurement. In addition, the signal intensity is proportional to the density of optical states, $D(\Delta\omega)$, obtained from the reflection spectrum.

Fitting our data to eq 1 (Figure 2, red dotted) proves inadequate because there is a large signal at high-energy Raman shifts greater than −2000 cm^{-1} that is not well described by the Bose−Einstein distribution. However, by adapting the method of Szczerbiński et al. our data are readily described if additional terms are included to account for a

DOI: 10.1021/acsenergylett.9b01857
ACS Energy Lett. 2019, 4, 2508−2513

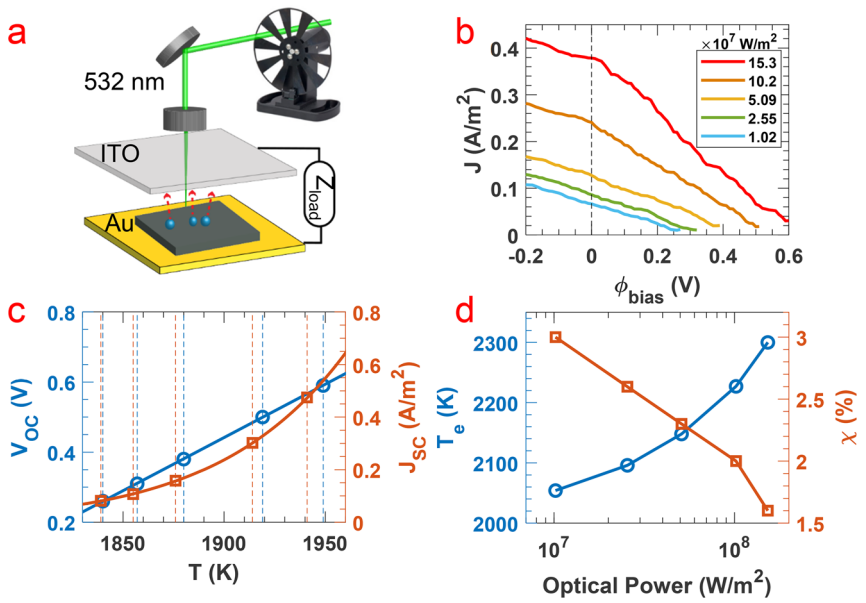

Figure 3. (a) Schematic of thermionic emission measurement. (b) $J-V$ curve measured at different optical powers. (c) Measured J_{SC} (square) and V_{OC} (circle) versus the calculated temperature according to a one-temperature model. The vertical dashed lines indicate the discrepancies in calculated temperature based on J_{SC} (red) or V_{OC} (blue). (d) Fitted electronic temperature (circle) and percentage of hot electrons χ (square) according to the two-temperature model of eq 3.

subpopulation of hot electrons, χ, with an energy distribution at an elevated temperature, T_e.[20]

$$I(\Delta\omega) = C * D(\Delta\omega) * \left(\frac{1-\chi}{e^{hc\Delta\omega/kT_l} - 1} + \frac{\chi}{e^{hc\Delta\omega/kT_e} + 1} \right) \quad (2)$$

The magnitude of χ in the steady state depends on both the generation rate of hot electrons due to optical excitation and the relaxation rate as electrons equilibrate to T_l via phonon scattering. Those carriers in thermal equilibrium with the lattice follow Bose–Einstein statistics, whereas the high-energy tail of the Raman signal is described by Fermi–Dirac statistics.[22] The fit to this two-temperature model (TTM) (Figure 2a, blue dashed line) is excellent for all optical powers probed, spanning 10^7 to 10^{11} Wm^{-2}. (See Figure S3 for more details.) However, it should be noted that the hot electron signal is fairly weak compared with the signal from the thermalized electron bath. Eliminating other sources of error and artifacts such as room lights as well as long integration times is required to obtain a good signal. We also cannot fully discount other small effects contributing to the signal that may result from changes in the optical response with temperature, such as shifts in the plasmon resonances of the nanostructures due to volume expansion. Nonetheless, we show later that the hot electrons can also be detected in electrical devices.

The dependence of T_e, T_l, and χ on optical power for the nanostructure was determined by analyzing the Raman spectra using eq 2. Samples were measured under vacuum (0.010 mbar). The fitted data are summarized in Figure 2b–d. Melting and degradation of the samples occurred when the fitted T_l significantly exceeded ~600 K in vacuum. We observed a monotonic increase in T_e and T_l as the optical power increased, with T_e in excess of T_l by at least an order of magnitude. This trend is expected due to the lower heat capacity of the electron gas,[13,23] and the values we measure for T_e and T_l are similar to those reported in transient absorption (TA) experiments[19] for comparable optical powers. To date, TA experiments have been the primary method for probing electron dynamics; however, our experiments also access lower optical powers than can be achieved in pulsed time-resolved studies.

A unique capability of our experiments that cannot be readily achieved in pulsed TA studies is the quantification of the size of the hot electron population, χ. An analysis of χ from our fitted spectra therefore provides important new information about how the availability of hot electrons depends on optical power and temperature under CW illumination that is more directly comparable to operating conditions for emerging hot-electron-based technologies. Interestingly in all experiments, we observe a clear inverse correlation between T_e and χ as optical power increases. One may initially expect that increases in optical power would lead to a greater rate of electronic excitation and thus a larger steady-state population of hot electrons. We hypothesize that the opposite behavior is due to the increase in electron–phonon coupling as temperature increases, providing faster relaxation of the hot electrons that overwhelms the increase in the excitation rate. Our hypothesis is supported later by an analysis of the thermionic emission from the nanostructure and is in agreement with TA measurements and computational studies of metal nanostructures.[22,24]

To demonstrate that the hot electrons can perform work, we constructed a thermionic power converter using the same nanostructure from Figure 1 as an emitter with an indium tin oxide (ITO) counter-electrode as a collector (Figure 3a). The current density, J, was measured via a lock-in amplification scheme from parallel electrodes separated by 200 μm during 532 nm CW illumination under vacuum (0.010 mbar); see the SI for further details. The power-generation region of the current–voltage ($J-V$) response is depicted in Figure 3b. The open-circuit voltage (V_{OC}) reported here represents the retarding bias at which the current density reaches the noise level for the lock-in amplifier (Figure S4b). The downward

DOI: 10.1021/acsenergylett.9b01857
ACS Energy Lett. 2019, 4, 2508–2513

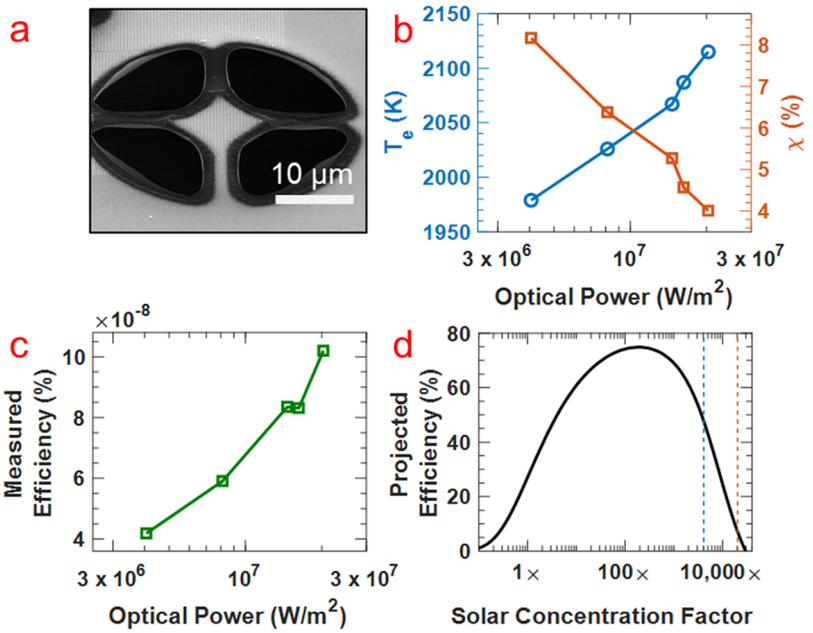

Figure 4. (a) SEM image of a thermally isolated gold nanostructure. (b) Fitted electronic temperature (circles) and percentage of hot electrons (squares) according to the two-temperature model of eq 3. (c) Measured optical power conversion efficiency and (d) projected optical power conversion as a function of solar concentration factor, assuming a decreased work function, W = 1.6 eV. The blue and red vertical dashed lines denote the range of low and high optical powers, respectively, probed experimentally in panels b and c.

curvature of the $J-V$ response indicates the presence of space charge effects during the measurement.[9]

The thermionic emission current density is conventionally described using Richardson's equation, which we adapted to accommodate a TTM. Because only a fraction of hot electrons, χ, at temperature T_e provide a non-negligible contribution to the thermionic current,

$$J = \chi A T_e^{\,2} e^{-(W+\phi_{bias}+\phi_{sc})/kT_e} \quad (3)$$

where A = 1.2017 × 10^7 Am^{-2} K^{-2} is the Richardson's constant, W = 5.1 eV is the work function of gold,[25] ϕ_{bias} is the external potential with the positive sign indicating a retarding bias, and ϕ_{SC} is the additional potential due to the electrostatic field of the space charge, calculated using Langmuir's space charge theory.[26] If we analyze our data assuming a one-temperature model, then the short-circuit current at zero bias, J_{SC}, and the V_{OC} measured from the $J-V$ response are inconsistent with a unique fitted temperature (Figure 3c). However, for each optical power probed there is a unique combination of T_e and χ that can be input into eq 3 to accurately reproduce both the experimentally measured J_{SC} and V_{OC}, as summarized in Figure 3d.

We find that T_e monotonically increased with optical power, with the same inverse relationship between χ and T_e measured in the Raman study above. We note that the relationship between T_e and χ may be different at even lower optical power regimes depending on the full temperature dependence of the electron−phonon coupling. Furthermore, the magnitude of χ is consistent with the Raman fitting under the same optical powers, although the fitted T_e based on the device response is somewhat lower. Several factors could give rise to this discrepancy, and we hypothesize that the largest source of error may be due to the more complex geometry of the space charge for electrons emitted by the nanostructure surface in comparison with the parallel plate geometry assumed in Langmuir's space charge theory.[26] (See the SI for more discussion.) In particular, the sharp corners of the nanostructure may generate a significantly larger fraction of vacuum-emitted electrons if emission is more likely where the optical field is locally concentrated. (See Figure S1b,c.) The result would be a greater space charge field near corners compared with a smooth surface. We note that the inverse correlation between T_e and χ is manifest independent of what analysis is used to model the space charge effect or other nonidealities not accounted for in eq 3. As an important point of comparison, we observed no measurable current under any optical power when a gold thin film was used as the emitter. This difference is likely due to a three-fold increase, at a minimum, in suitable escape cones for hot electrons in the nanocubes and highlights how momentum constraints are relaxed in the plasmonic nanostructure. Whereas we expect that the size of the nanostructures may play a crucial role in the generation rate and efficiency of hot electron emission, based on recent computational studies, we expect that the dynamics of the hot electrons for both the nanostructures and the thin film are dominated by surface scattering processes.[22]

To demonstrate the potential of this strategy for solar power conversion, an additional sample was prepared that minimized losses due to conduction. The nanostructure was fabricated on a 50 nm thick Si_3N_4 membrane. Focused ion beam etching was used to perforate the membrane and thermally isolate a 6 × 6 μm section of the array (Figure 4). In vacuum, the device achieved optical power conversion efficiency between 10^{-8} and 10^{-7}% under 4 × 10^6 to 2.1 × 10^7 Wm^{-2}. This optical power range is comparable to that employed in solar−thermal conversion schemes, where solar concentration factors are commonly between 1500× and 4000×. Whereas the sample showed no evidence of thermal degradation, the seemingly low efficiency is due to the large work function of gold, W = 5.1 eV. It is common practice during thermionic device operation to include rarified Cs metal vapor to both decrease W via surface adsorption and minimize space charge effects. Gold surfaces

DOI: 10.1021/acsenergylett.9b01857
ACS Energy Lett. 2019, 4, 2508−2513

with submonolayer cesium have a reported work function of W = 1.6 eV.[27] At low current density, the emitted electrons do not remove enough energy from the system to significantly perturb the electronic and lattice temperature, similar to a theoretical scenario in which no current is emitted and all optical power goes to photothermalization. Thus the $J-V$ response we measured provides a calibration that relates both the electronic temperature and the population of hot electrons at a given incident optical power (Figure S7). Assuming that the presence of Cs does not significantly alter the plasmonic response of the absorber when the decreased work function is present, a maximum conversion efficiency of 74.9% is predicted to occur at 190× solar concentration based on the trade-off between T_e and χ. If practically achievable, such high efficiency for collecting hot electrons would significantly decrease the optical energy that is available to promote heating of the lattice through electron−phonon coupling, further promoting the stability of the emitter. See the SI for more details of this calculation. For comparison, state-of-the-art solar−thermal conversion strategies commonly achieve ∼30% efficiency at lattice temperatures greater than 1000 K.[28]

In conclusion, we have demonstrated a new optoelectronic power conversion mechanism that uses plasmonic nanostructures to decouple electronic temperature and lattice temperature during the steady-state optical illumination of a thermionic emitter. We have also developed an optical thermometry technique based on anti-Stokes Raman spectroscopy to quantify these separate temperatures as well as the size of the subpopulation of hot electrons. Our results show an inverse relationship between the temperature and the population of the hot electron gas. When integrated into thermionic devices, the plasmonic cathodes provide optical power conversion efficiency consistent with the electronic temperature while maintaining significantly lower lattice temperatures. Thus we demonstrated how this mechanism can overcome challenges related to thermal stability that have historically limited the use of thermionic devices for solar-thermal energy conversion. We believe the remarkable tailorability of plasmonic nanostructures may allow further opportunities for very efficient solar energy conversion based on this strategy.

■ ASSOCIATED CONTENT

Supporting Information

The Supporting Information is available free of charge on the ACS Publications website at DOI: 10.1021/acsenergylett.9b01857.

Methods, field enhancement map, Raman spectra, fitting procedures, electrical measurement, and projected efficiency calculation (PDF)

■ AUTHOR INFORMATION

Corresponding Author

*E-mail: sheldonm@tamu.edu.

ORCID

Shengxiang Wu: 0000-0002-1173-5569

Matthew Sheldon: 0000-0002-4940-7966

Notes

The authors declare no competing financial interest.

■ ACKNOWLEDGMENTS

This work is funded by the Air Force Office of Scientific Research under award number FA9550-16-1-0154. M.S. also acknowledges support from the Welch Foundation (A-1886).

■ REFERENCES

(1) Brongersma, M. L.; Halas, N. J.; Nordlander, P. Plasmon-Induced Hot Carrier Science and Technology. *Nat. Nanotechnol.* **2015**, *10*, 25.

(2) Knight, M. W.; Sobhani, H.; Nordlander, P.; Halas, N. J. Photodetection with Active Optical Antennas. *Science* **2011**, *332*, 702.

(3) Wu, S.; Sheldon, M. T. Optical Power Conversion Via Tunneling of Plasmonic Hot Carriers. *ACS Photonics* **2018**, *5*, 2516.

(4) Linic, S.; Christopher, P.; Ingram, D. B. Plasmonic-Metal Nanostructures for Efficient Conversion of Solar to Chemical Energy. *Nat. Mater.* **2011**, *10*, 911.

(5) Zhou, L.; Swearer, D. F.; Zhang, C.; Robatjazi, H.; Zhao, H.; Henderson, L.; Dong, L.; Christopher, P.; Carter, E. A.; Nordlander, P.; Halas, N. J. Quantifying Hot Carrier and Thermal Contributions in Plasmonic Photocatalysis. *Science* **2018**, *362* (6410), 69.

(6) Mukherjee, S.; Libisch, F.; Large, N.; Neumann, O.; Brown, L. V.; Cheng, J.; Lassiter, J. B.; Carter, E. A.; Nordlander, P.; Halas, N. J. Hot Electrons Do the Impossible: Plasmon-Induced Dissociation of H2 on Au. *Nano Lett.* **2013**, *13* (1), 240−247.

(7) Leenheer, A. J.; Narang, P.; Lewis, N. S.; Atwater, H. A. Solar Energy Conversion Via Hot Electron Internal Photoemission in Metallic Nanostructures: Efficiency Estimates. *J. Appl. Phys.* **2014**, *115* (13), 134301.

(8) Narang, P.; Sundararaman, R.; Atwater, H. A. Plasmonic Hot Carrier Dynamics in Solid-State and Chemical Systems for Energy Conversion. *Nanophotonics* **2016**, *5* (1), 96−111.

(9) Hatsopoulos, G. N.; Gyftopoulos, E. P. *Thermionic Energy Conversion*; MIT Press: Cambridge, MA, 1973.

(10) Xiao, G.; Zheng, G.; Qiu, M.; Li, Q.; Li, D.; Ni, M. Thermionic Energy Conversion for Concentrating Solar Power. *Appl. Energy* **2017**, *208*, 1318−1342.

(11) Schwede, J. W.; Bargatin, I.; Riley, D. C.; Hardin, B. E.; Rosenthal, S. J.; Sun, Y.; Schmitt, F.; Pianetta, P.; Howe, R. T.; Shen, Z. X.; Melosh, N. A. Photon-Enhanced Thermionic Emission for Solar Concentrator Systems. *Nat. Mater.* **2010**, *9* (9), 762−7.

(12) Segev, G.; Rosenwaks, Y.; Kribus, A. Limit of Efficiency for Photon-Enhanced Thermionic Emission Vs. Photovoltaic and Thermal Conversion. *Sol. Energy Mater. Sol. Cells* **2015**, *140*, 464−476.

(13) Jiang, L.; Tsai, H.-L. Improved Two-Temperature Model and Its Application in Ultrashort Laser Heating of Metal Films. *J. Heat Transfer* **2005**, *127* (10), 1167−1173.

(14) Grubisic, A.; Schweikhard, V.; Baker, T. A.; Nesbitt, D. J. Coherent Multiphoton Photoelectron Emission from Single Au Nanorods: The Critical Role of Plasmonic Electric near-Field Enhancement. *ACS Nano* **2013**, *7* (1), 87−99.

(15) Cialla, D.; März, A.; Böhme, R.; Theil, F.; Weber, K.; Schmitt, M.; Popp, J. Surface-Enhanced Raman Spectroscopy (Sers): Progress and Trends. *Anal. Bioanal. Chem.* **2012**, *403*, 27−54.

(16) Edward, I.; Solomon, A. B. P. L. *Inorganic Electronic Structure and Spectroscopy*; John Wiley & Sons, Inc.: 1999; Vol. *I*.

(17) Cai, Y.-Y.; Sung, E.; Zhang, R.; Tauzin, L. J.; Liu, J. G.; Ostovar, B.; Zhang, Y.; Chang, W.-S.; Nordlander, P.; Link, S. Anti-Stokes Emission from Hot Carriers in Gold Nanorods. *Nano Lett.* **2019**, *19* (2), 1067−1073.

(18) Xie, X.; Cahill, D. G. Thermometry of Plasmonic Nanostructures by Anti-Stokes Electronic Raman Scattering. *Appl. Phys. Lett.* **2016**, *109* (18), 183104.

(19) Huang, J.; Wang, W.; Murphy, C. J.; Cahill, D. G. Resonant Secondary Light Emission from Plasmonic Au Nanostructures at High Electron Temperatures Created by Pulsed-Laser Excitation. *Proc. Natl. Acad. Sci. U. S. A.* **2014**, *111* (3), 906.

DOI: 10.1021/acsenergylett.9b01857
ACS Energy Lett. 2019, 4, 2508−2513

(20) Szczerbiński, J.; Gyr, L.; Kaeslin, J.; Zenobi, R. Plasmon-Driven Photocatalysis Leads to Products Known from E-Beam and X-Ray-Induced Surface Chemistry. *Nano Lett.* **2018**, *18* (11), 6740−6749.
(21) Carattino, A.; Caldarola, M.; Orrit, M. Gold Nanoparticles as Absolute Nanothermometers. *Nano Lett.* **2018**, *18* (2), 874−880.
(22) Singh, N. Two-Temperature Model of Nonequilibrium Electron Relaxation: A Review. *Int. J. Mod. Phys. B* **2010**, *24* (09), 1141−1158.
(23) Lin, Z.; Zhigilei, L. V. Thermal Excitation of D Band Electrons in Au: Implications for Laser-Induced Phase Transformations. *Proc. SPIE* **2006**, *6261*, 62610U.
(24) Brown, A. M.; Sundararaman, R.; Narang, P.; Goddard, W. A.; Atwater, H. A. Ab Initio Phonon Coupling and Optical Response of Hot Electrons in Plasmonic Metals. *Phys. Rev. B: Condens. Matter Mater. Phys.* **2016**, *94* (7), 075120.
(25) Ford, R. R.; Pritchard, J. Work Functions of Gold and Silver Films. Surface Potentials of Mercury and Xenon. *Trans. Faraday Soc.* **1971**, *67* (0), 216−221.
(26) Hatsopoulos, G. N.; Gyftopoulos, E. P. *Thermionic Energy Conversion, Vol. II: Theory, Technology, and Application*; MIT Press: Cambridge, MA, 1979.
(27) LaRue, J. L.; White, J. D.; Nahler, N. H.; Liu, Z.; Sun, Y.; Pianetta, P. A.; Auerbach, D. J.; Wodtke, A. M. The Work Function of Submonolayer Cesium-Covered Gold: A Photoelectron Spectroscopy Study. *J. Chem. Phys.* **2008**, *129* (2), 024709.
(28) Siva Reddy, V.; Kaushik, S. C.; Ranjan, K. R.; Tyagi, S. K. State-of-the-Art of Solar Thermal Power Plants—a Review. *Renewable Sustainable Energy Rev.* **2013**, *27*, 258−273.

DOI: 10.1021/acsenergylett.9b01857
ACS Energy Lett. 2019, 4, 2508−2513